DETACHED AND LARGE EDDY SIMULATION OF UNSTEADY SIDE-LOADS OVER AN AXISYMMETRIC AFTERBODY

Sébastien Deck, Eric Garnier

ONERA, Applied Aerodynamics Department, BP72, F-92322 Châtillon Cedex FRANCE

ABSTRACT

The main purpose of this paper is to assess the capability of DES and LES methods to calculate unsteady side-loads encountered on a generic launcher afterbody. A comparison with the available experimental data including spectral analysis of pressure fluctuations with or without jet are given. The unsteady properties of the computed side loads are then discussed. Despite an overestimation of the pressure fluctuations on the emergence, the computations are able to recover the predominant frequency at a Strouhal number of 0.2. Moreover, the jet suction effect on the emergence pressure distribution is well predicted. The two points analysis has demonstrated the occurrence of highly coherent antisymmetrical wall pressure fluctuations on the emergence surface. With or without jet, the side-loads can be interpreted as a rotating vector uniformly distributed in the range $[0; 2\pi]$ and whose magnitude follows Rayleigh's law.

Key words: DES; LES; afterbody; side-loads.

1. INTRODUCTION

Massive, highly unstable separation occurs in the flow over the afterbody of a launch vehicle where the flow is subject to unsteady three-dimensionnal phenomena. Flow separation is a highly three-dimensionnal process which can result in dynamic loads (also called side-loads) and might disturb the stability of the flight. Moreover, these fluctuations can excite a response of the structural modes called buffeting. The design of afterbodies of future launch vehicles needs a better knowledge of the unsteady flow mechanisms involved in the buffet phenomenon. Since unsteady buffet loads are difficult to measure experimentally, computational methods are becoming of growing interest in space launcher design. In particular, Detached and Large Eddy Simulation offer interesting perspectives for an accurate description of these flows. The main purpose of this paper is the evaluation of those methods in a generic afterbody configuration for which experimental data are available [1]. The objective of the present effort is twofold: 1) to assess the capability of DES and LES to simulate the separated flow over an axisymmetric afterbody 2) to analyze the main features of the flowfield as well as the properties of the unsteady side-loads.

2. TURBULENCE MODELLING

Fluctuations of instantaneous flow characteristics (pressure, vorticity,...) depend both on space and time. They occur over a wide range of scales. The smaller scales (so-called Kolmogorov scales) are settled by the fluid viscosity while the largest are the most often linked to the geometry of the problem (diameter of the base, nozzle exit,...). Practical turbulent flows presented in this paper exhibit such a wide range of excited length and time scales (shock wave, boundary and free shear layers,...) at high Reynolds number that Direct Numerical Simulations (DNS) are not reachable for the foreseeable future. Classical methods such as Reynolds Averaged Navier-Stokes (RANS) equations are not able to provide any information about the unsteadiness of these flows. Conversely, Detached and Large Eddy Simulations (DES and LES respectively) are well adapted to handle massive separated flows or free shear layers encountered on the base.

2.1 zonal-Detached Eddy Simulation (DES)

Detached Eddy Simulation (DES) was proposed by Spalart et al.[2] and has given encouraging results for a wide range of flow configurations exhibiting massive separations [3, 4, 5, 6]. The motivation for this approach was to combine the best features of Reynolds Averaged Navier Stokes approach with the best features of Large Eddy Simulation. RANS tends to be able to predict attached flows very well with a low computational cost. On the other hand, LES has a high computational cost but can predict separated flows more accurately. The DES treatment of turbulence is aimed at the prediction of separated flows at unlimited Reynolds numbers and at a reasonable cost.

The model was originally based on the Spalart-Allmaras RANS model which solves a one equation turbulence model for the eddy viscosity $\tilde{\nu}$:

$$\frac{D\rho\tilde{\nu}}{Dt} = c_{b1}\tilde{S}\rho\tilde{\nu} + \frac{1}{\sigma}\left(\nabla.(\mu+\rho\tilde{\nu})\nabla\tilde{\nu} + c_{b2}\rho(\nabla\tilde{\nu})^2\right) - \rho c_{w1} f_w \left(\frac{\tilde{\nu}}{d}\right)^2 \quad (1)$$

The eddy viscosity is defined as

$$\mu_t = \rho\tilde{\nu} f_{v1} = \rho\nu_t, \quad f_{v1} = \frac{\chi^3}{\chi^3 + c_{v1}^3}, \quad \chi = \frac{\tilde{\nu}}{\nu} \quad (2)$$

The f_w and $f_v's$ functions are near-wall correction functions in the finite Reynolds number version of the model and we refer to the original papers [7, 8] for details on the constants and the quantities involved. For the current research, the transition terms were turned off.

What is important here is that the model is provided with a destruction term for the eddy viscosity that contains d, the distance to the closest wall. This term when balanced with the production term, adjusts the eddy viscosity to scale with local deformation rate $\tilde{S}$ producing an eddy viscosity given by

$$\tilde{\nu} \sim \tilde{S} d^2 \tag{3}$$

Following these arguments, Spalart et al. suggested to replace d with a new length $\tilde{d}$ given by

$$\tilde{d} = min\,(d, C_{DES}\Delta) \tag{4}$$

where $\Delta = max\,(\Delta_x, \Delta_y, \Delta_z)$ is the computational mesh size. The use of the maximum grid extension is physically justified as it controls which wavelengths can be resolved and the eddy-viscosity level. More precisely, in the attached boundary layer, due to the significant grid anisotropy ($\Delta_x \approx \Delta_z \gg \Delta_y$) typical of this flow region, in accordance with (4), $\tilde{d} = d$, and the model reduces to the standard SA RANS model. Otherwise, once a field point is far enough from walls ($d > C_{DES}\Delta$), the length scale of the model performs as a subgrid-scale version of the SA model.

However, standard DES introduces a significant dependency into the RANS part of the simulation which requires a grid spacing for the wall grid in tangential direction that is larger than the boundary layer thickness at that location. This grid resolution may be easily violated in the present study for the incoming boundary layer on the cylinder. More precisely, if the switching in LES mode occurs inside the RANS boundary layer, this will result in an underestimation of the skin friction coefficient[9, 10]. To avoid this problem in the incoming attached boundary-layer, we used a "zonal-DES" approach[11] where attached boundary layer regions are explicitly treated in RANS mode regardless to the grid resolution.

2.2 Large Eddy Simulation (LES)

In LES, the large-scale field is computed directly from the solution of the filtered (local volume-averaged) Navier-Stokes equations, and the small scale stresses are modeled. The SGS model then represents the effects of the small scales on the large-scale motions. Assuming that these small scales have mainly a dissipative effect, a Boussinesq approximation is used and a SGS viscosity has to be specified. The later one is computed with the Selective Mixed Scale Model which reads

$$\nu_t = C_m f_s \left|\widetilde{S}\right|^{\alpha} \left(q_c^2\right)^{\frac{(1-\alpha)}{2}} \Delta^{(1+\alpha)} \tag{5}$$

with

$$q_c{}^2 = \frac{1}{2}(\widetilde{u}_k - \widehat{\widetilde{u}}_k)^2$$

The test filter $\widehat{\ }$ is derived from the trapezoidal rule, α is set to 0.5 and the parameter $C_m = C_m(\alpha)$ is found equal to 0.1. The selection function tests the tridimensionality of the flow to avoid the application of the model in non-turbulent zone. This model is presented as a low computational cost alternative to dynamic models, since it simply takes into account the local structure of the flow by computing the kinetic energy of the highest resolved frequencies q_c^2.

2.3 Numerical method

The solver FLU3M code has been developed by ONERA. It solves the Navier Stokes equations on multi block structured grids. The computational domain is divided by blocks ; each block is composed of structured hexahedral cells. The Navier Stokes equations are discretized using a second order accurate upwind finite volume scheme and a cell centered discretization. The Euler fluxes are discretized by a modified AUSM+(P) upwind scheme, which is fully described in Ref.[12]. This scheme is used for the configuration without jet whereas Roe's flux difference splitting scheme is used to compute the configuration with jet.
Unsteady (global time-step) and three dimensional Navier-Stokes simulations are highly CPU demanding. Explicit schemes are not efficient enough for this purpose and implicit schemes are required. Time discretization is based on second-order accurate Gear's formulation and has been introduced in FLU3M by Péchier[13] during his thesis. Moreover, the implicit formulation results in inversion of a large sparse matrix system. The LU factorization simplifies the inversion of the latter implicit system. Further details concerning the numerical method and implementation of turbulence models can be found in references[13, 14].
This numerical method is the same as the one already used to perform LES of the flow around a two-dimensional wing profile in near-stall conditions[12] as well as around a low pressure turbine blade [15] and has also been successfully used to compute LES of the flow over a cavity at high Reynolds number [16] and to compute zonal-DES of transsonic buffet over a supercritical airfoil [11].

3. TEST CASE

3.1 ONERA experiment

The general configuration is a base flow prolongated by an emergence of lower diameter. A nozzle is lo-

cated in this emergence. Experiments can be performed either with jet or without jet. The figure 1 presents an enlargement of the computational domain in the base region. An exemple of the isoMach number contours in the nozzle is given in figure 2. The length and the diameter of the emergence are respectively 60 % and 40 % of the base diameter.

The experiments were performed in the atmospheric S3ch wind tunnel of the ONERA Meudon center. The Mach number was fixed to 0.7 and in the case with jet, the ratio of the jet pressure over the external pressure is equal to 34.2.

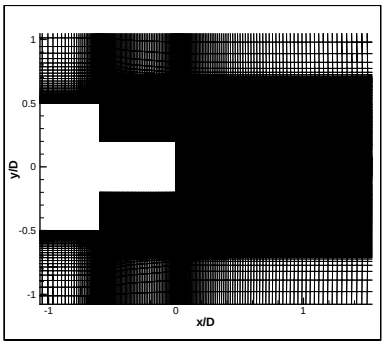

Figure 1. Description of the configuration

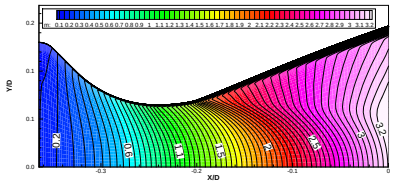

Figure 2. Iso-Mach number contours in the nozzle

3.2 Grids and description of the computations

The first case without jet is computed with both DES and LES whereas the case with jet is treated only with DES. In all cases, the number of grid points is about 5 millions. Nevertheless, the grid points distributions is different between LES and DES. In the latter, the mesh is particularly refined in the longitudinal direction whereas in the former the circonferential distribution of grid points is favored. In both cases, a good cell isotropy in the emergence is achieved. A view of the mesh in the longitudinal direction is shown in figure 1. The figure 3 gives an idea of the mesh refinement in a transverse plane located at the nozzle exit for the DES computation with jet. Furthermore, it is worth noting that, in all computations, the inflow boundary layer profile is a RANS profile matching the experimental data.

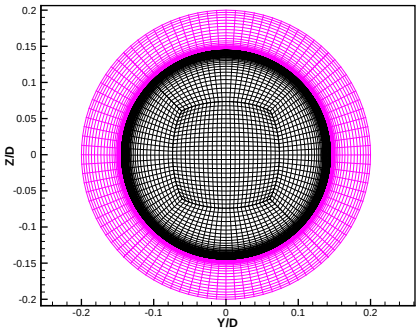

Figure 3. DES grid in the nozzle exit section (black)

4. RESULTS-DISCUSSION

4.1 Flowfield description

4.1.1 Without jet

A figure showing the main characteristics of the instantaneous flowfield is presented in Figure 4. The turbulent structures are exhibited showing a positive iso-value of the criterion $\mathcal{Q}$ [17]. It defines as vortex tubes the regions where the second invariant of velocity gradient tensor $\mathcal{Q}$ is positive :

$$\mathcal{Q} = \frac{1}{2}\left(\Omega_{ij}\Omega_{ij} - S_{ij}S_{ij}\right) = -\frac{1}{2}\frac{\partial u_i}{\partial x_j}\frac{\partial u_j}{\partial x_i} > 0 \qquad (6)$$

where S_{ij} and Ω_{ij} are the symmetric and antisymmetric components of ∇u, respectively.

This picture clearly shows the roll-up of toroïdal eddies which are destabilized by azimuthal instability modes. After the break-up of these toroïdal eddies, the main structures appear to be longitudinal eddies. The same value of $\mathcal{Q}$ has been plotted for the DES and LES calculation. The LES calculation exhibits more structures because the LES grid is finer in the azimuthal direction ($N_z = 97$ for the DES grid and $N_z = 177$ for the LES grid). The eddies in the mixing layer dividing the trapped recirculating flow behind the base and the external flow is also displayed figure 5. This figure also highlights a second mixing layer emanating from the corner at the end of the rear body. The unsteady simulation is averaged in time during the calculation. Figure 6 compares to experiment the streamwise evolution of the pressure coefficient on the afterbody between RANS, DES and LES. One can notice that the experiment is characterized by a slow decay of Cp as the streamwise location increases. No recompression process on the afterbody is evidenced. That means that there is no reattachment of the shear layer on the surface. The averaged value of the mean pressure coefficient on the afterbody is equal to $C_p \approx -0.14$. This important characteristic of the Cp distribution is not well

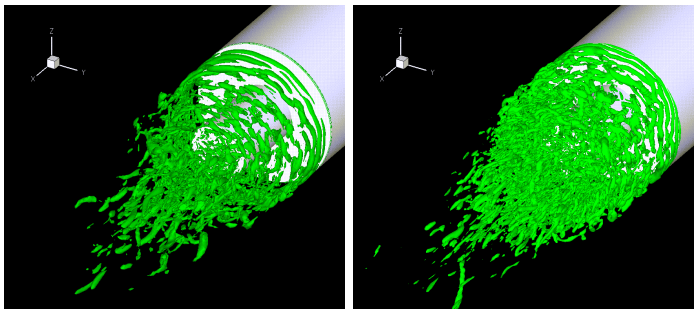

Figure 4. Instantaneous view of coherent structures educed using Q criterion (left view:DES ; right view: LES)

Figure 5. Instantaneous pseudo-schlieren view ($||\nabla\rho||$ DES calculation)

reproduced by the RANS calculation with Spalart-Almaras turbulence model[7, 8] whereas DES and LES are in better agreement with experiment. Nevertheless, the LES calculation exhibits a pressure drop at the end of the afterbody which was associated in the calculation to reattachement bubble. This pressure drop is not observed experimentally.

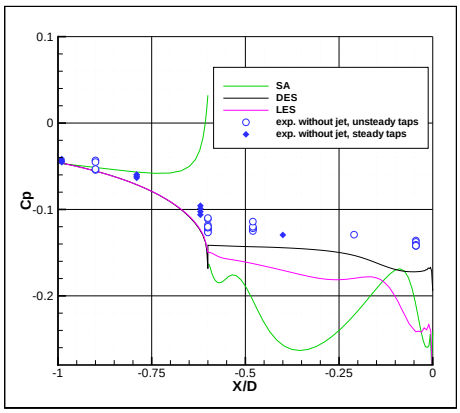

Figure 6. Streamwise distribution of pressure coefficient

4.1.2 With jet

The presence of the supersonic jet strongly modifies the flow topology due to the interaction of this jet with the external separated flow. The resulting flow description of the instantaneous flowfield in presence of a jet is given in figure 7. One can particularly notice the roll-up of toroïdal eddies which are destabilized by azimuthal instability modes. The interaction of these eddies with the supersonic jet is complex. The recompression shock in the supersonic jet issued from the nozzle is clearly visible on the instantaneous Schlieren-like illustration. Figure 8 presents

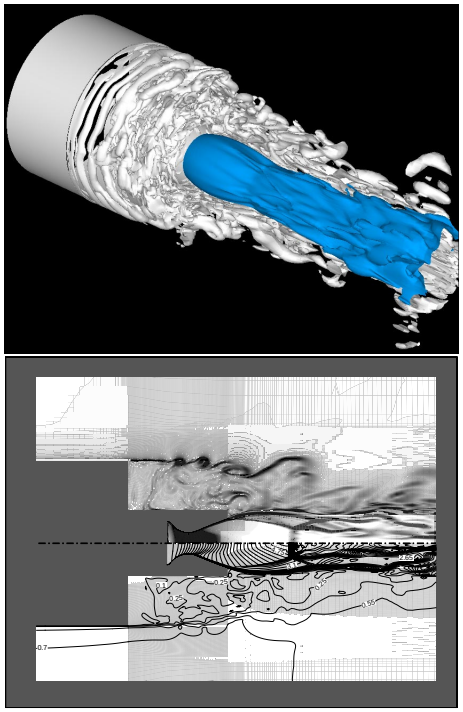

Figure 7. Top : surface iso $-$ $Q > 0$ (grey) et sonic surface (blue)-DES computation ; Bottom : instantaneous Schlieren-like visualisation

the effect of the jet on the streamwise evolution of the pressure coefficient. One can notice that the base pressure is decreased compared to the case without jet. This behaviour is known to be produced by the suction effect of the jet shear layer which tends to empty the external recirculation region. The DES calculation reproduces this effect but underestimate the suction effect of the jet.

4.2 Pressure fluctuation

4.2.1 Spectral analysis

Once separation occurs, the flow looses its axisymmetrical nature which leads to pressure pulsation, that is, an unsteady nature of the separated flow. In this section, the most energetic frequencies involved in the flow unsteadiness is investigated. The Power Spectral Density function, named $G(f)$, describes how the mean squared value of the wall pressure is distributed in frequency[18]. The PSD is then

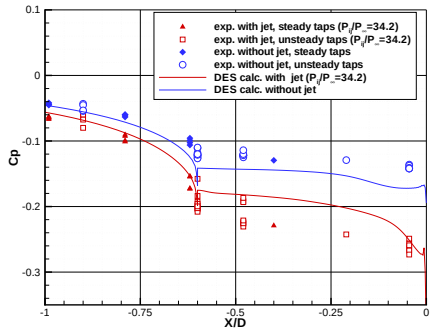

Figure 8. Streamwise distribution of pressure coefficient (DES calculations)

normalized by $\frac{Dq_\infty^2}{U_\infty}$ so that :

$$C_{prms} = \int_0^\infty G\left(St_D\right) d\left(St_D\right) = \int_0^\infty St_D.G\left(St_D\right) d\left(\log St_D\right) \quad (7)$$

As suggested by Depres[1, 19], the spectra are plotted as $\sqrt{St_D G\left(St_d\right)}$. Figure 9 compares to experiment the pressure spectra on the after-body obtained by DES and LES for the configuration without jet. For the case without jet, the experimental spectrum displays a sharp peak at a normalized frequency of about $St_D \approx 0.2$. The near wake flow is characterized by a global unsteadiness and the periodicity is attributed to the vortex shedding of large scale turbulent structures as observed for several axisymmetric bodies [20, 21, 22]. The occurrence of the peak at $St_D \approx 0.2$ is reproduced by the calculation especially for the LES calculation but the level of fluctuation is too large for the LES calculation compared to the experimental value. In case of an adapted supersonic jet, this peak is less evidenced. Indeed, the presence

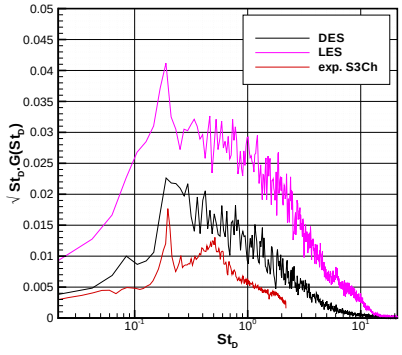

Figure 9. Pressure spectra on the rear body at $X/D = -0.05$ without jet

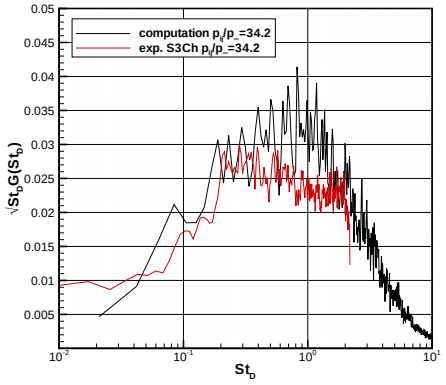

Figure 10. Pressure spectra on the rear body at $X/D = -0.05$ with jet (DES calculation))

of the jet may be seen as an obstacle to the development of turbulent structures. The resulting sharp increase of the pressure fluctuation levels at the end of the afterbody appears to result from broad band contribution at very high frequencies. These high frequencies fluctuations can be associated to the interaction of the separated shear layer with the supersonic jet. It is also worth noting that the spectrum obtained by DES compares favorably with experiments.

4.2.2 Two-point analysis

The spectral analysis has highlighted an important contribution of the normalised frequency $St_D \approx 0.2$. To evidence the resulting spectral contribution to side-load, one can study the spatial organization of the flow at this frequency. This can be achieved by considering the azimuthal coherence of two pressure transducers $p_1\left(r, X, \phi_1\right)$ and $p_2\left(r, X, \phi_1\right)$ located in a normal plane to the inflow $X = constant$. Assuming the hypothesis of an homogeneous flow, the complex coherence function may be expressed as :

$$C\left(f, r, X, \Delta\phi\right) = \left(C_r + jC_i\right)\left(f, r, X, \Delta\phi\right) = \frac{G_{12}\left(f, r, \Delta\phi, X\right)}{\sqrt{G_1\left(f, r, X, \phi_1\right) G_2\left(f, r, X, \phi_2\right)}} \quad (8)$$

where G_{12} is the cross-spectral density, $\Delta\phi = \phi_1 - \phi_2$. The coherence can be defined by $\gamma(f) = |C(f)|$ and $\Phi(f)$ the coherence phase angle between p_1 and p_2 at frequency f.

Figure 11 compares to experiment, the curve $\gamma\left(\Delta\phi\right)$ at $X/D = -0.05$ at the vortex shedding frequency. A classical turbulence flowfield should normally result in a monotonous decrease of the coherence with the distance between the two-transducers. In the present situation, the coherence effectively decreases in the range $[0, 90\,deg]$ to reach a minimum near $\Delta\phi = 90\,deg.$ but increases again in the range $[90; 180\,deg.]$.

In addition, this behaviour of the coherence function is associated with an anti-phase relationship of the signals for $\Delta\phi = 180\,deg$. The occurrence of highly coherent antisymmetric wall pressure fluctuations on the rear body surface is of primary importance in the assessment of buffet loads. These important features of the spatial flow organization are well reproduced by DES and LES. Figure 12 then presents the effect

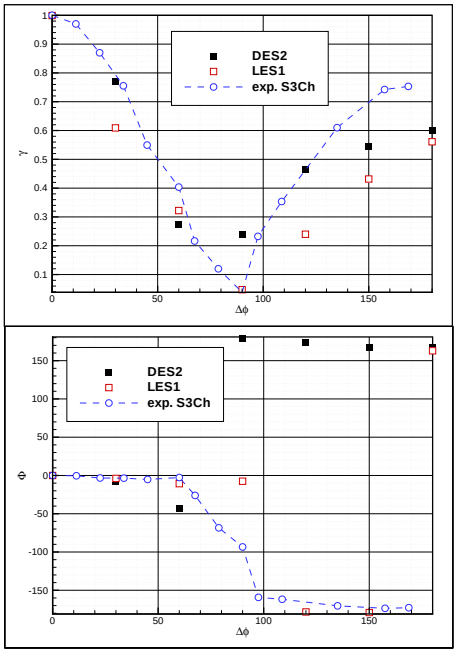

Figure 11. Circumferential coherence distribution and phase angle coherence Φ at frequency $St_D \approx 0.2$ $(X/D = -0.05$, without jet, DES and LES)

of the jet on the flow organization and compares to experiment the DES calculation. The particular azimuthal correlation of the wall fluctuations still exists although more weakly defined as in the case without jet (see Fig. 11). This result suggest some less organised flow structure at frequency $St_D \approx 0.2$ due to the separated flow interaction with the jet.

5. SIDE-LOADS ASSESSMENT

Downstream of the base, the flow does not remain uniform. The separation has an unsteady and three-dimensional behaviour which leads to non-symmetrical pressure loads on the wall. Figure 13 shows a typical plot, $F_z(t)$ versus $F_y(t)$ of computed buffet loads for the configuration with jet obtained with the zonal-DES approach. These loads are obtained by integrating the pressure field on the rear body surface during the calculation. One can notice the isotropic and random character of the fluctuating side-load. Side-loads description can be achieved either with a polar description $(F(t), \theta(t))$ or with a carthesian description using its components on Y, Z axis. The two descriptions are linked by the following

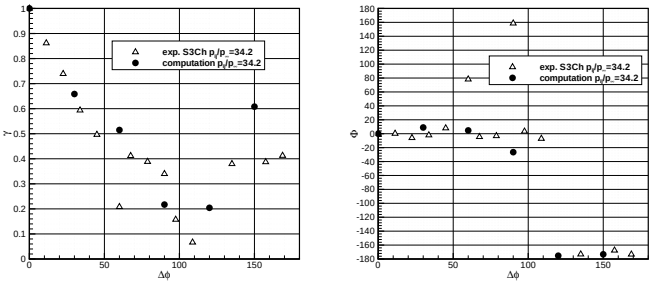

Figure 12. Circumferential coherence distribution and phase angle coherence Φ at frequency $St_D \approx 0.2$ $(X/D = -0.05mm$, with jet, DES)

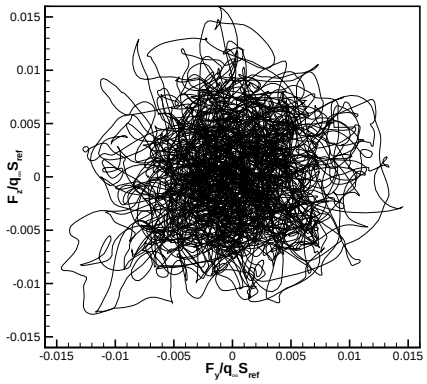

Figure 13. Computed polar plot of buffet load (with jet, DES calculation)

relations:

$$\begin{cases} F(t) &= \sqrt{F_y^2(t) + F_z^2(t)} \\ \theta(t) &= Atg\left(\frac{F_y(t)}{F_z(t)}\right) \end{cases} \tag{9}$$

To complete and define properties of magnitude and direction of the side-loads caused by random pressure fluctuations, a statistical description is needed. There are numerous ways to define probability, but from an engineering point of view, the most convenient definition is in term of relative frequency of occurrence. Indeed, it is interesting to take into account the probability density function of the side-load magnitude and direction. The computed side-force probability density function is compared in the cases with and without jet in figure 14. Firstly, it is worthwhile to note that the presence of the jet does not modify statistical properties of the side-load magnitude. Both values indicate that the distribution of side-load amplitude is a *Rayleigh* distribution whose probability density function is described with

the following relation:

$$\begin{cases} p(F|\lambda) & = \frac{F}{\lambda^2} e^{-\frac{F^2}{2\lambda^2}}, \quad x \geq 0 \\ 0 & otherwise \end{cases} \tag{10}$$

where F is the random value of the side-load amplitude and λ a parameter which is taken equal to $\lambda = \sqrt{\frac{1}{2N}\sum_{i=1}^{N} F_i^2}$ (Most Likely Hood Estimator) and N is the size of the sample.

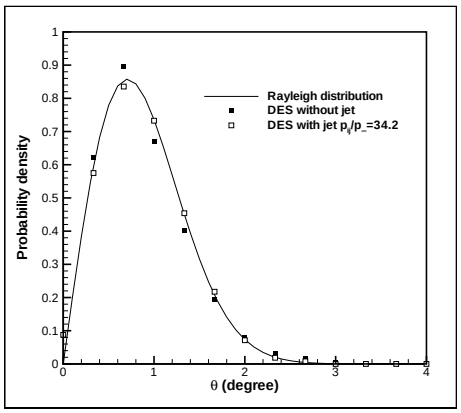

Figure 14. Pdf of side-load amplitude (DES calc.)

These results could be quite expected for an axisymmetrical geometry since the Rayleigh distribution is the particular case of a χ^2 distribution with two degrees of freedom which correlatively means that the side-loads components are normally distributed.

To evaluate if the computational time is long enough to get correct statistical properties of side-loads, a first criteria is to qualify the statistical isotropy of the computed side-load since for an axisymmetrical geometry, no particular direction has to be privileged (See Ref [23]). Afterwards, figure 15 compares to the uniform law the computed probability density function of the side-load direction with and without jet. One can notice that with or without jet, the experimental and computed Pdf of side-load direction are fluctuating around the uniform law within the interval $[0; 2\pi]$ (or $[0; 360]$ *degree*) defined by

$$\begin{cases} p(\theta) = \frac{1}{2\pi}, \quad 0 < x \leq 2\pi \\ 0 \quad otherwise \end{cases} \tag{11}$$

Finally, the calculations suggest that with or without jet, the side-loads can be seen as a rotating vector uniformly distributed within the interval $[0; 2\pi]$ and whose magnitude follows Rayleigh's law.

Figure 16 finally presents the PSD of the $F_y(t)$ component in the case with or without jet. It is worth

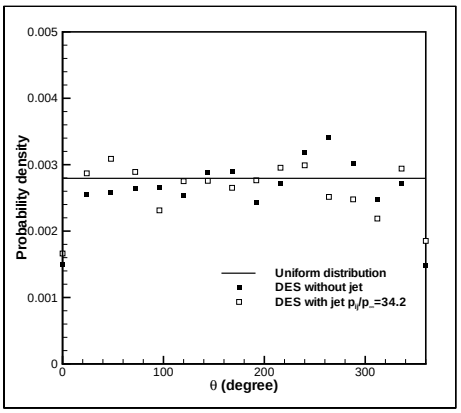

Figure 15. Pdf of side-load direction (DES calc.)

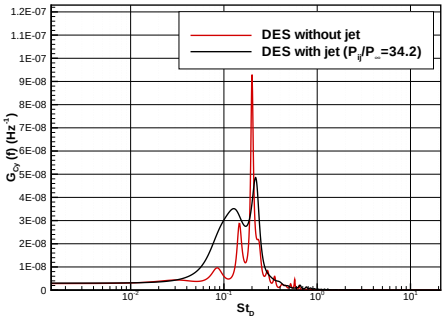

Figure 16. Effect of the jet on the PSD of F_y side-load component

noting the important contribution of the frequency $St_D \approx 0.2$ for the case without jet. This peak is still exhibited in presence of a supersonic jet but is less pronounced. This result corroborates with the two-point analysis, e.g., the pressure field on the rear body surface is strongly anti-correlated at the frequency $St_D \approx 0.2$ (see figures 11 and 12).

6. CONCLUSION

Both DES and LES were used to investigate in details the flow behind an axisymmetrical afterbody. Despite an overestimation of the pressure fluctuations on the emergence, the computations are able to recover the predominant frequency at a Strouhal number of 0.2. Moreover, the jet suction effect on the emergence pressure distribution is well predicted. The two points analysis has demonstrated the occurrence of highly coherent antisymmetrical wall pressure fluctuations on the emergence surface. With or without jet, the side-loads can be interpreted as a rotating vector uniformly distributed in the range $[0; 2\pi]$ and whose magnitude follows Rayleigh's law. Further work will be dedicated to the assessment of DES and LES for geometries more representative of a those of realistic launcher afterbodies.

Acknowledgments

The authors are greatly indebted to MM. Depres and Reijasse from ONERA for supplying the experimental data and their colleagues, MM. Hallard and Guillen from ONERA are warmly acknowledged for fruitful discussions. This study is partly funded by CNES within the framework of the CNES Research and Technology Program ATAC (Aerodynamics of nozzles and afterbodies) under technical cooperation between CNES/ONERA/CNRS/SNECMA and EADS-LV.

REFERENCES

[1] D. Depres. *Analyse physique et modélisation des instationnarités dans les écoulements d'arrière-corps transoniques*. PhD thesis, Université de la Méditerranée Aix-Marseille II, 2003.

[2] P. Spalart, W.H. Jou, M. Stretlets, and S.R. Allmaras. Comments on the feasibility of LES for wings and on a hybrid RANS/LES approach. *In Proceedings pp 137-147, 1st AFSOR Int. Conf. on DNS/LES, Ruston*, 1998.

[3] M. Strelets. Detached Eddy Simulation of Massively Separated Flows. *AIAA Paper 01-0879, 39th AIAA Aerospace Sciences Meeting and Exhibit, Reno, Nevada*, 2001.

[4] K.D. Squires, J.R. Forsythe, S.A. Morton, W.Z. Strang, K.E. Wurtzler, R.F. Tomaro, M.J. Grismer, and P.R. Spalart. Progress on Detached-Eddy Simulation of Massively Separated Flows. *AIAA Paper 02-1021, 40th AIAA Aerospace Sciences Meeting and Exhibit, Reno, Nevada*, 2002.

[5] J.R. Forsythe, K.D. Squires, K.E. Wurtzler, and P.R. Spalart. Detached-Eddy Simulation of Fighter Aircraft at High Alpha. *AIAA Paper 02-0591, 40th AIAA Aerospace Sciences Meeting and Exhibit, Reno, Nevada*, 2002.

[6] S. Deck, E. Garnier, and P. Guillen. Turbulence modelling applied to space launcher configurations. *Journal of Turbulence, vol.3, (57), pp 1-21, (http://jot.iop.org)*, 2002.

[7] P.R. Spalart and S.R. Allmaras. A one equation turbulence model for aerodynamic flows. *AIAA Paper 92-0439*, 1992.

[8] P.R. Spalart and S.R. Allmaras. A one equation turbulence model for aerodynamic flows. *La Recherche Aérospatiale,pp 5-21*, 1994.

[9] N.V. Nikitin, F. Nicoud, B. Wasistho, K.D. Squires, and P.R. Spalart. An approach to wall modeling in large eddy simulation. *Physics of Fluids, vol.12, pp 1629-1631*, 2000.

[10] B. Caruelle. *Simulations d'Écoulements Instationnaires Turbulents an Aérodynamique: Application à la prédiction du phénomène de tremblement*. PhD thesis, Institut National Polytechnique de Grenoble, 2000.

[11] S. Deck. Detached Eddy Simulation of transonic buffet over a supercritical airfoil. *AIAA Paper 04-5378, 22nd AIAA Applied Aerodynamics Conference, Providence, Rhode Island, August*, 2004.

[12] I. Mary and P. Sagaut. Large eddy simulation of flow around an airfoil near stall. *AIAA J., vol.40, No.6, pp 1139-1145*, 2002.

[13] M. Péchier, Ph. Guillen, and R. Caysac. Magnus Effect Over Finned Projectiles. *AIAA Journal of Spacecraft and Rockets, vol.38, No.4, pp. 542-549*, 2001.

[14] S. Deck, Ph. Duveau, P. d'Espiney, and Ph. Guillen. Development and application of spalart allmaras one equation turbulence model to three-dimensional supersonic complex configurations. *Aerospace Science and Technology, Vol. 6, No. 3, pp 171-183*, 2002.

[15] B. Raverdy, I. Mary, P. Sagaut, and Liamis N. High-resolution large-eddy simulation of the flow around a low pressure turbine blade. *AIAA J., vol.41, No.3, pp 390-397*, 2003.

[16] L. Larchevêque, O. Labbé, I. Mary, and P. Sagaut. Les of a compressible flow past a deep cavity. *Physics of Fluids, vol.15, No.1 , pp 193-210*, 2003.

[17] Delcayre F. Dubief Y. On coherent-vortex identification in turbulence. *Journal of turbulence, vol. 1, number 11*, 2000.

[18] J.S. Bendat and A.G. Piersol. Random data: Analysis and measurements procedures. *Wiley-Interscience, New-York*, 1971.

[19] D. Depres and P. Reijasse. Experimental study of wall pressure in afterbody flows with and without jet. *AIAA Paper 03-3469*, 2003.

[20] J.P. Flodrops and J.M. Desse. Sillage d'un culot axisymétrique. *Onera/IMFL, Rappport No.85/19*, 1985.

[21] D. Depres. Synthèse bibliographique : aspects instationnaires des écoulements décollés et application aux phénomènes d'écoulements de culot. *Onera, RT No.65/06143 DAFE ou RT-NT-4224ATACACO-0001-ONER-01*, 2001.

[22] H.V. Fuchs, E. Mercker, and U. Michel. Large scale coherent structures in the wake of axisymmetric bodies. part 1. the feedback phenomenon. *Journal of Fluid Mechanics, vol.93, pp 185-207*, 1979.

[23] S. Deck and A.T. Nguyen. Unsteady Side Loads in a Thrust Optimized Contour Nozzle at Hysteresis regime. *AIAA Journal, vol.42, No.9, pp 1878-1888*, 2004.